ACS APPLIED ENERGY MATERIALS

www.acsaem.org Article

High-Performance and Low-Cost Overhead Projector Sheet-Based Triboelectric Nanogenerator for Self-Powered Cholesteric Liquid Crystal, Electroluminescence, and Portable Electronic Devices

Supraja Potu, Navaneeth M, Rakesh Kumar Rajaboina,* Buchaiah Gollapelli, Jayalakshmi Vallamkondu, Siju Mishra, Haranath Divi, Anjaly Babu, Uday Kumar K, and Prakash Kodali

Cite This: *ACS Appl. Energy Mater.* 2022, 5, 13702−13713 Read Online

ACCESS | Metrics & More | Article Recommendations | Supporting Information

ABSTRACT: Low output power, intricate device designs, limitation on scalability, limited production capability, and higher fabrication cost are the major hurdles to use triboelectric nanogenerators (TENGs) as a power source in self-powered device applications. This work reports a high-performance, simple design, and inexpensive TENG using overhead projector (OHP) sheets and ZnO nanosheet array films. The fabricated TENG produced a maximum output voltage, current, and power density of ∼292 V, ∼55 μA, and ∼424.8 mW/m^2 for each hand slapping force, respectively. The charged nature of one side of the OHP sheet is responsible for obtaining the high-power density reported in this communication. Further, the TENG has shown excellent stability over a period of 6 months and more than 10,000 test cycles. The stability of ZnO nanosheets is excellent even the after 10,000 test cycles. The TENG's AC output is utilized to control the optical characteristics of the cholesteric liquid crystal (CLC) devices. CLC devices are demonstrated for mobile security, optical switch, webcam security, and self-powered smart windows or e-paper displays. Further, we have demonstrated self-powered electroluminescence and portable electronic devices. The current work has potential applications in portable, wearable, and self-powered electronic devices due to its high power density, simple design, minimal cost, and scalability.

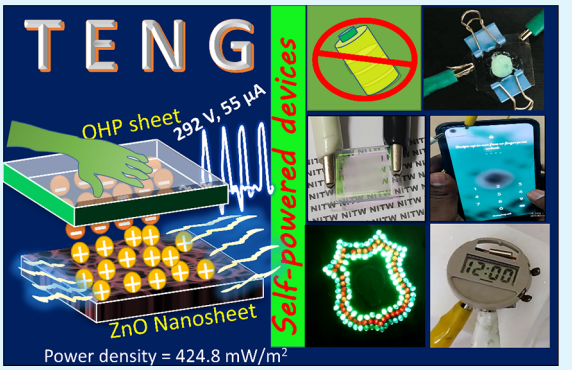

KEYWORDS: *self-powered devices, triboelectric nanogenerator, mechanical energy harvesting, ZnO nanosheets array, cholesteric liquid crystal*

1. INTRODUCTION

In recent years, triboelectric nanogenerators (TENGs) have gained intense attention owing to their diverse applications in energy harvesting,[1] self-powered sensors,[2] self-powered medical devices,[3] self-powered health monitoring,[3] electrochromic devices,[4] electroluminescence devices,[5] optical modulation,[6] electromechanical systems,[7] and e-paper.[8] TENGs convert a variety of mechanical energies in our daily life into electricity by utilizing the combined effect of contact electrification and the electrostatic induction phenomenon. Until the discovery of the TENG in 2012, contact electrification was treated as an undesirable effect.[9] After that, the field of TENGs has rapidly progressed due to their high output voltages, high energy conversion efficiency, broad material availability, low cost, easy device fabrication, high flexibility, and environmental friendliness.[10] However, there are significant challenges encountered by TENGs: (i) low output power, (ii) applications of TENGs in limited fields due to low output power, and (iii) no product commercialization due to the use of complex TENG designs. Specific strategies have been proposed in the literature to overcome the above challenges and enhance the TENG's output power. These strategies were proposed based on the governing equations of the TENG's output voltage, current, and charge.[11−13]

The first strategy attempts to increase the surface charge density as it is directly related to the current, voltage, output energy, and power of TENGs. The surface charge density can be increased by selecting new materials, which have high surface charge density from the triboelectric series[14] or any materials (e.g., oxides and nitrides) from the periodic table and polymers.[15−17] In addition, surface modification, which includes physical modification,[18,19] chemical surface functionalization,[20−23] and surface ion injection,[24−26] is also considered for

Received: July 25, 2022
Accepted: October 18, 2022
Published: October 31, 2022

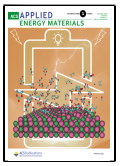

https://doi.org/10.1021/acsaem.2c02359
ACS Appl. Energy Mater. 2022, 5, 13702−13713

Table 1. List of Pairing Materials that Formed the TENG with ZnO Nanostructure Films and Their Output Voltage, Current, Power/Power Density, and Explored Applications

Sl. no.	ZnO tribolayer	pairing tribolayer	voltage (V_{oc})	current (I_{sc})	power/power density(PD)	demonstrated applications	ref
1	PVDF + ZnO nanowires	Nylon + ZnO	330 V	10 μA	3 W/m^2	168 series LEDs directly,power up thermometer with a charged capacitor	36
2	PDMS + Ag + ZnO nanotubes	aluminum		10 μAcm^{-2}	1.1 mW/cm^2	switched on 99 LEDs	37
3	Al-doped ZnO + graphene oxide	polyimide	105 V	2.85 μAcm^{-2}	2.5 W/m^2	switched on 60 series-connected LEDs	38
4	ZnO nanorods	PDMS	5.34 V	181.4 nA		no application	39
5	chitosan + ZnO	PDMS	0.9 V		24.5 nW	acetone sensing	40
6	ZnO nanorods + polystyrene	Kapton	7 V	0.99 nA	230 μW/cm^2	no application	41
7	ZnO nanosheets	PET	4.9 V	10 μA	1 μW/cm^2	power up watch, 24 LEDs with a charged capacitor	42
8	bacterial cellulose + ZnO	Teflon	57.6 V	5.78 μA	42 mW/m^2	no applications	43
9	ZnO nanoparticles	Kapton	57 V	1.21 μA	2.8 1 μW/cm^2	power up watch, calculator with a charged capacitor	44
10	ZnO nanosheets	ITO	~2 V	6 μA	4.15 μW	no applications	45
11	ZnO + PVDF	PTFE	78 V	0.46 μAcm^{-2}	24.5 μW/cm^2	no applications	46
12	ZnO nanostrctures	polymide	31.6 V	5.43 μA		no applications	47
13	ZnO nanoripples	polymide	~80 V	0.8 μA	1.13 W/m^2	no applications	48
14	Sb-doped ZnO	PDMS	12 V	20 nAcm^{-2}		no applications	49
15	PDMS + ZnO	PTFE	64.2 V	6.1 mAm^{-2}	1105 mW/m^2	switched on 30 LEDs	50
16	ZnO + PDMS	ITO/PET	6 V		4.8 μW/cm^2	power up thermometer with a charged capacitor	51
17	ZnO nanosheets	overhead projector(OHP) sheet	292 V	~55 μA	~424.8 mW/m^2	self-powered CLC, EL, portable electronic devices	presentwork

the surface charge density increment. Furthermore, the performance of the TENG's output can also be improved by filling some special fillers into the triboelectric layers.[27−29] The optimization of particulate fillers can effectively improve the charge trapping ability and improve the TENG's output. In other strategies, increasing the effective contact area between the frictional layers enhances the TENG charge output. Increasing the effective contact area includes the use of liquid/gel electrodes[30] and soft structures.[31]

In this manuscript, we have used the pre-charged triboelectric layer for a high-performance triboelectric nanogenerator with cost-effective materials and explored applications of the TENG in new fields. This study introduced a new triboelectric pair of overhead projector (OHP) sheets and ZnO nanosheet arrays on aluminum foil to fabricate the TENG device. The OHP sheet is a transparent material made up of PET, and it has a pre-charge on one side to receive the ink particles. The existence of charge on the OHP sheets greatly enhances the TENG performance and also reduces the surface ion injection step.[24] The cost of OHP sheets is very low compared to the other triboelectric layers such as PTFE, PVDF, silicone, and FEP. We have performed a simple test to confirm the charged nature of the OHP (PET) sheets in contrast to normal PET sheets. In the test, small paper pieces were placed on a table, and the OHP sheet and PET sheet were placed close to the paper pieces. The OHP attracted paper pieces, whereas the PET sheet did not attract any paper pieces, as shown in Figure S1a,b and Video S1, Supporting information. Further, both sides of the OHP sheet were tested to confirm the presence of a charge on them. It was clear from the test that one side of the OHP is strongly attracting a large number of paper pieces, whereas another side does not attract many, as shown in Figure S2a,b and Video S2. Therefore, we can expect high output voltage and current from only one side of the OHP sheet. Table 1 shows the existing ZnO-based TENGs with different tribomaterials, their output performance, and applications. We have limited our comparison literature table to the ZnO-based systems since we have used the ZnO-OHP(PET) system.

The ZnO-OHP-based TENG and its application in self-powered cholesteric liquid crystal (CLC) and electroluminescence devices have not been reported in the literature so far. The present investigation is the first of its kind, and it opens up new possibilities with the ZnO-based TENG. The self-powered liquid crystal displays and electroluminescence devices have received limited attention in the literature due to the high power required to turn on these devices. In the present work, we have studied the optical responses of electroluminescent and CLC devices in various applications using AC voltage produced by the fabricated TENG devices.

Recently, the research group of Wang et al. reported TENG-driven cholesteric liquid crystal devices and their application in information security, smart windows, optical switches, e-paper displays, and wireless sensors.[32−35] To the best of the authors' knowledge, these are the only four reports available in the literature on TENG-driven cholesteric liquid crystals. The present manuscript also reports a similar application using TENG-driven cholesteric liquid crystal devices but with additional advantages. The advantages include the simple design of the TENG without any additional modifications to the conventional design process such as patterning of tribolayers. The aluminum foil, ZnO, OHP sheets, cardboards, and sponge spacers involved in the TENG fabrications make it a cost-effective design. The typical 5 × 5 cm^2 TENG device fabrication costs only $2.05 (Table S1).

https://doi.org/10.1021/acsaem.2c02359
ACS Appl. Energy Mater. 2022, 5, 13702−13713

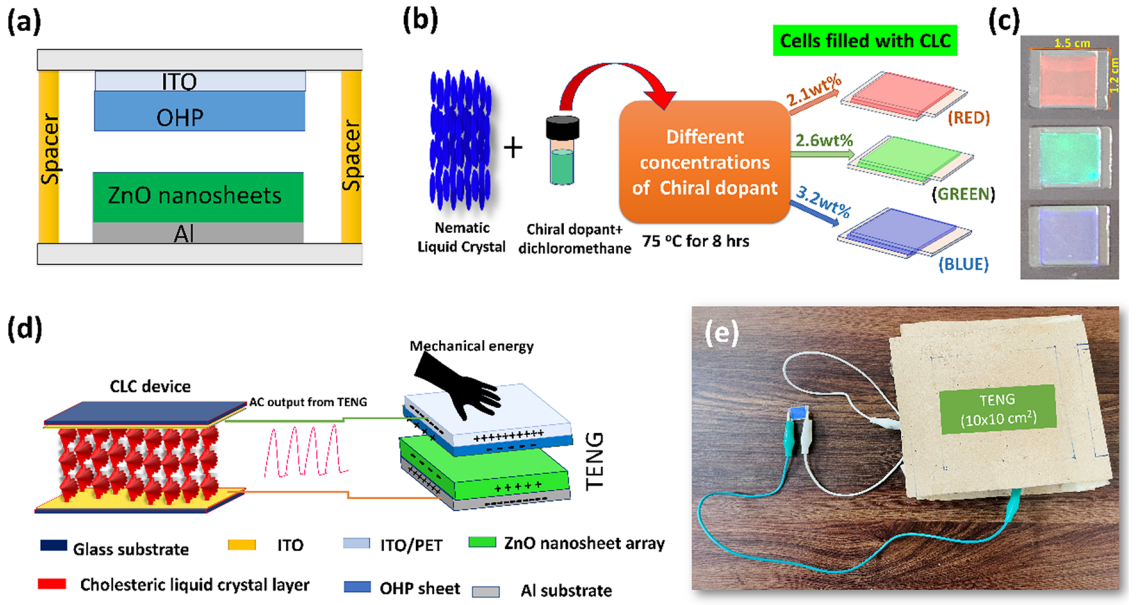

Figure 1. (a) Schematic representation of the TENG device and its components, (b) schematic view of the fabrication of the different colored CLC devices, (c) photographs of the original CLC devices on a black background, (d) schematic view of the TENG-integrated CLC device, and (e) photograph of the actual CLC device integrated with the TENG.

This study reports a high-performance TENG using the ZnO nanosheet film and OHP sheet as frictional layers. The fabricated TENG has been characterized by its output current, voltage, power, and stability. The TENG performance has been studied with different device sizes, under the different frequencies of applied force and magnitudes of applied force. In addition, the TENG has been explored for self-powered device applications.

2. EXPERIMENTAL DETAILS

2.1. Materials. Zinc nitrate hexahydrate ($Zn(NO_3)_2$), hexamethylenetetramine (HMTA), and ITO/PET (60 Ω/sq.) were purchased from Sigma-Aldrich. Aluminum foils were acquired from Special Metals Pvt. Ltd. Overhead projector (OHP) sheets/slides of ∼100 μm were obtained from a local market shown in Figure S3. The nematic liquid crystal E7 (n_e = 1.741, n_o = 1.517 at 589 nm; T_{NI} = 59 °C) and right-handed chiral dopant R5011 (HCCH, helical twisting power HTP = 107 μm^{-1}) were obtained from Sigma-Aldrich.

2.2. ZnO Nanosheets Synthesis Procedure. The simple and low-cost hot plate-assisted hydrothermal method was adopted to obtain ZnO nanosheets, similar to our previous reports.[52,42] First, the ZnO precursor solution was prepared by dissolving a 1:1 ratio of zinc nitrate hexahydrate and HMTA precursors in 100 mL of DI water. A clean aluminum substrate (6 cm × 6 cm) was kept vertically in the growth solution beaker and placed on a hot plate for 4 h at 85 °C growth solution temperature. After the reaction, the aluminum substrate appeared white in color due to the formation of a ZnO coating. Furthermore, ZnO films were characterized and used for the fabrication of TENG devices. The details of the ZnO nanosheet synthesis schematic and the characterization are found in Figure S4.

2.3. Fabrication and Testing of the TENG Devices. The schematic view of the TENG device is shown in Figure 1a, and detailed fabrication steps are presented in Figure S5. In the TENG, the ZnO nanosheet array and OHP sheet (charged side) were used as frictional layers, and ITO and aluminum substrates were used as conductive electrodes. The OHP sheet was attached to the conducting side of ITO with more charged side facing up. Two electrical connections were made from the bottom aluminum and top ITO electrode to record the TENG response. The fabricated TENG was tested periodically under vertical contact separation mode by applying a hand slapping force of ∼6.12 N. The hand slapping force was calculated approximately using the reported procedure in the literature.[53,19] The TENG device's open-circuit voltage and short-circuit current were measured using a digital storage oscilloscope (Tektronix, TBS-1102) and a low noise current pre-amplifier SR 570 (Stanford Research Systems). The long-term stability of the TENG devices was tested for more than 10,000 cycles with an in-house modified linear motor shown in Figure S6. The vertical contact separation mode is selected among the four working modes due to its high output power density compared to the other working modes and less physical damage to the tribolayers than the lateral sliding and free-standing mode.[54,55]

2.4. Preparation of Different Color CLC Devices and Testing with the TENG. The nematic LC material (E7) was mixed with the chiral dopant R5011 to obtain mixtures with different concentrations of the dopant in dichloromethane as a solvent. Chiral dopant concentrations of 2.1, 2.6, and 3.2 wt % were used, allowing the CLC cells to reflect red (R), green (G), and blue (B) regions, respectively. To obtain homogeneous mixtures, these mixtures were stirred on a magnetic stirrer at a temperature of 80 °C (above the isotropic temperature) for 8 h. The mixtures were filled into the as-purchased LC cells by capillary action in the isotropic phase above a clearing point of E7 (∼59 °C). The LC cell comprises two ITO-coated glass substrates treated with a polymide layer and rubbed in antiparallel directions. The gap between two substrates is 5 μm with an active electrode area of 0.6 × 0.6 cm^2. The schematic of the fabrication process and photographs of the fabricated CLC devices are shown in Figure 1b and Figure 1c, respectively. Initially, CLC cells were placed on a black background. They exhibited red, green, and blue reflection colors with wavelengths of 630, 532, and 465 nm, respectively, corresponding to the added chiral dopant concentrations, as shown in Figure 1c.

The schematic of the TENG connected to the CLC device is shown in Figure 1d. The AC output of the TENG device is used for the molecular reorientation in the CLC device to change its optical properties. The AC signal generated by the TENG device upon the application of mechanical force is given as an input to the CLC device to transform its state. Depending on the magnitude of the AC signal, the CLC device may transform to more than one state. The photograph of the TENG (10 × 10 cm^2) device integrated with the CLC is shown in Figure 1e.

https://doi.org/10.1021/acsaem.2c02359
ACS Appl. Energy Mater. 2022, 5, 13702−13713

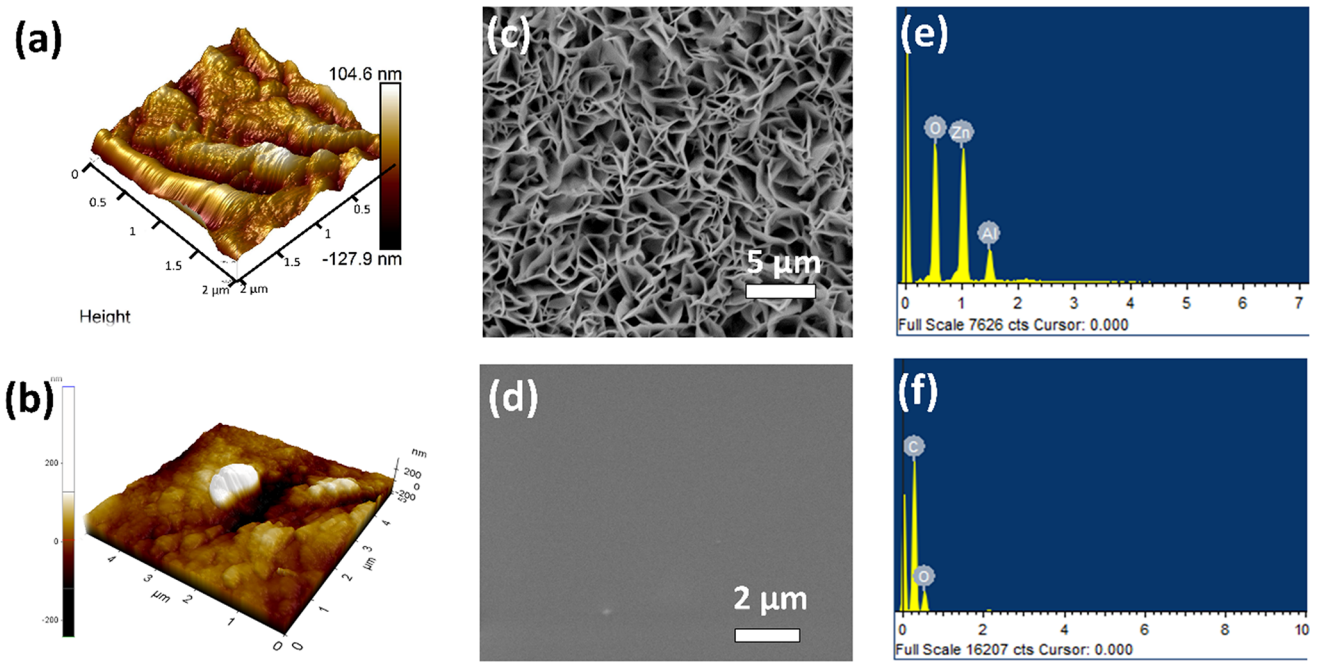

Figure 2. Topographical images of the (a) ZnO nanosheet film and (b) OHP sheet, morphological images of the (c) ZnO nanosheet film and (d) OHP sheet, and EDX spectra of the (e) ZnO nanosheet film and (f) OHP sheet.

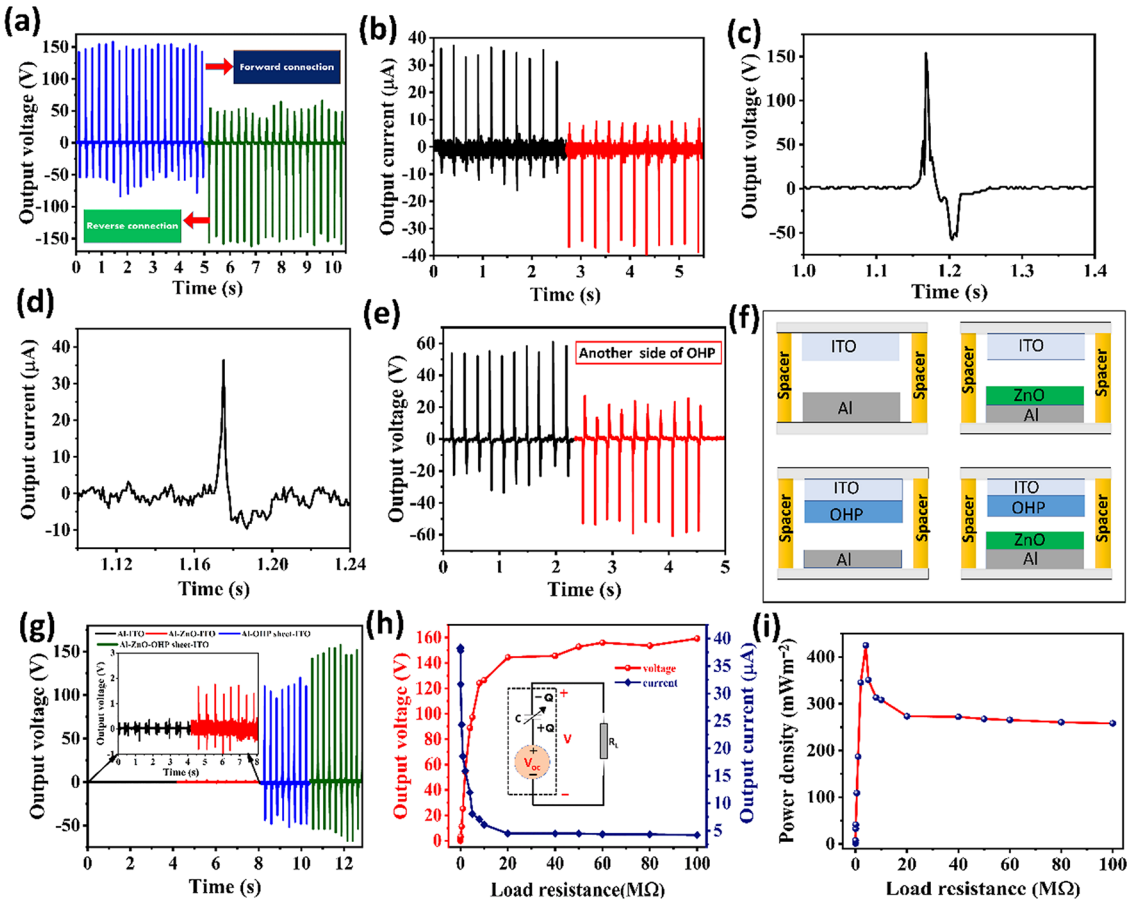

Figure 3. Electrical characteristics of the TENG (5×5 cm^2). (a) Open-circuit voltage in forward and reverse connections and (b) short-circuit current in forward and reverse connections, (c, d) magnified view of open-circuit voltage and short-circuit current of TENG response in one cycle, (e) TENG response with another side of the OHP sheet surface, (f) schematic of TENGs with different tribo-pairs, (g) TENG responses with different tribo-pairs of Al-ITO, ZnO-ITO, Al-OHP, and ZnO-OHP, (h) plot of output voltage and current with different load resistances, and (i) instantaneous power density with the load resistance.

https://doi.org/10.1021/acsaem.2c02359
ACS Appl. Energy Mater. 2022, 5, 13702−13713

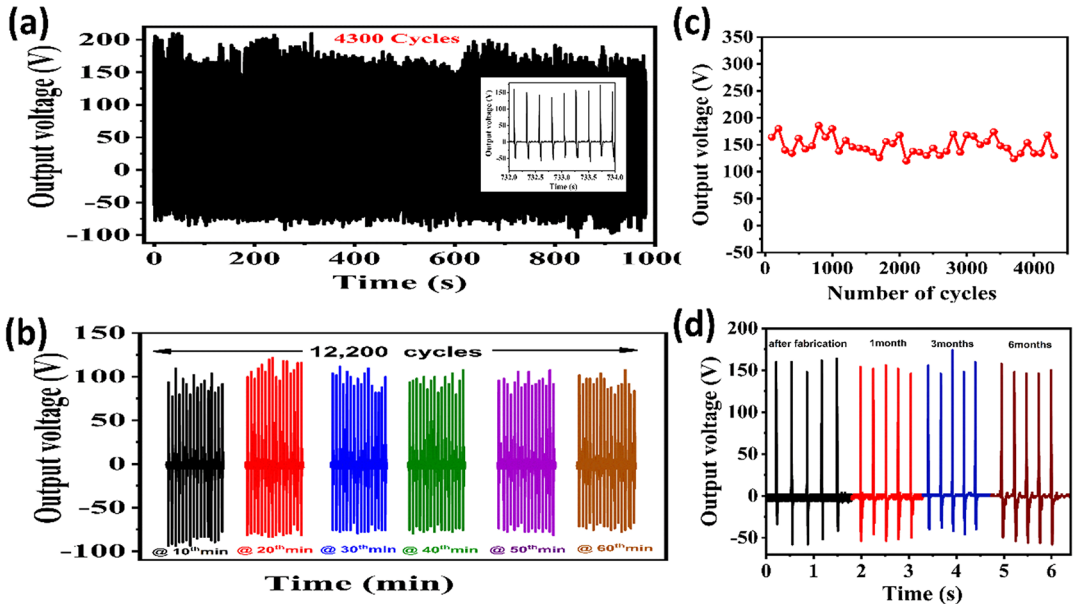

Figure 4. Stability of the TENG; (a) 4300 cycles with hand slapping (inset: few cycles from the stability graph), (b) 12,220 cycles with the linear motor, (c) TENG output voltage vs number of cycles, and (d) stability test of the TENG over a period of 6 months.

3. RESULTS AND DISCUSSION

Figure 2a and Figure 2b show the AFM images of the ZnO nanosheet film and the OHP sheet surfaces, respectively. The surface of the ZnO film has greater roughness than the OHP sheet due to the presence of the ZnO nanosheets. This rough surface of the ZnO film forms a more effective contact area to get the high output power to the TENG.

In addition, we analyzed the surface of frictional layers with SEM, and the corresponding images are shown in Figure 2c,d. The SEM images corroborate the AFM results of the low and high roughness of the OHP sheet and the ZnO nanosheet film. EDX spectra recorded from the ZnO nanosheet film and OHP sheet are shown in Figure 2e and Figure 2f, respectively. The EDX spectrum confirms the existence of Zn, O, and Al in the case of ZnO nanosheets on aluminum foil and C and O in the OHP sheet. The XRD and FTIR characterization details of the OHP and ZnO nanosheet films can be seen in Figure S7.

A simple hand slapping force was used on TENG devices (5 × 5 cm^2) to investigate mechanical energy harvesting. The open-circuit voltage (V_o) and short-circuit current (I_s) of the TENG against repeated hand slapping pressure were recorded and are presented in Figure 3a and Figure 3b, respectively. The V_o and I_s of the TENG device are ∼150 V and ∼34.5 μA, respectively. The observed values are significantly higher than the previously reported values for the ZnO-PET-based TENG by our group.[42] This enhancement is due to the pre-charged nature of the OHP sheets compared to the normal PET sheets. We have verified the V_o and I_s of the six TENG devices fabricated under identical conditions and found the same response. The V_o and I_s were measured as part of the switching polarity test to confirm the origin of the electrical signal.[56] In the switching polarity test, the V_o and I_s were measured under reversed electrical connections to the measuring device. From the switching polarity test (Figure 3a,b), it appears that V_o and I_s come from the TENG devices, not from noise. The magnified view of the open-circuit voltage and short-circuit current of TENG response in one cycle is presented in Figure 3c,d.

Further, the TENG was made with another OHP sheet purchased from different vendor and found a similar response of V_o and I_s shown in Figure S8. We fabricated one more TENG while keeping other side (non-charged) of the OHP as a frictional layer to understand the effect of the ink-receiving layer (charged) side on the TENG performance. The response of this new TENG is shown in Figure 3e, and the output voltage is reduced to ∼55 V, indicating that the charged side of the OHP significantly affects the output voltage. Figure 3f,g shows the measured V_o of different TENG devices: (i) without ZnO and OHP (ITO-Al), (ii) without the OHP (ITO-ZnO), (iii) without the ZnO nanosheet layer (OHP-Al), and (iv) with ZnO and OHP (ZnO-OHP). It is evident from Figure 3g that the OHP and ZnO frictional layers play a significant role in enhancing the output voltage.

The working mechanism of the contact separation mode TENG is very well elucidated in the literature based on triboelectrification and electrostatic induction.[1,9] A similar mechanism is adopted for the proposed TENG and presented in Figure S9. This model consists of an OHP sheet as a one triboelectric layer and the ZnO nanosheet film as another a triboelectric layer attached with ITO/PET and aluminum electrodes, respectively. The TENG is in equilibrium in the initial state since there is no contact between ZnO and the OHP sheet. When these layers contact each other under external force, they exchange electrons based on their electron affinities. The ZnO and OHP sheets carry the same quantity of opposite charges, resulting in equilibrium. When the external force is removed, the electrical potential is induced between the top and bottom electrodes. This potential difference drives the electrons (current) from one electrode to another until an equilibrium is reached. The induced electrostatic charges flow back (current) in the reverse direction when the external force is reapplied. The repeated application and removal of force produce an AC electrical output. Therefore, an alternating current is generated by continuous contact and separation movements.

To study the instantaneous output power of the TENG device (5 × 5 cm^2), the V_o and I_s were measured at different load resistance values ranging from 1 KΩ to 100 MΩ. With increasing

https://doi.org/10.1021/acsaem.2c02359
ACS Appl. Energy Mater. 2022, 5, 13702−13713

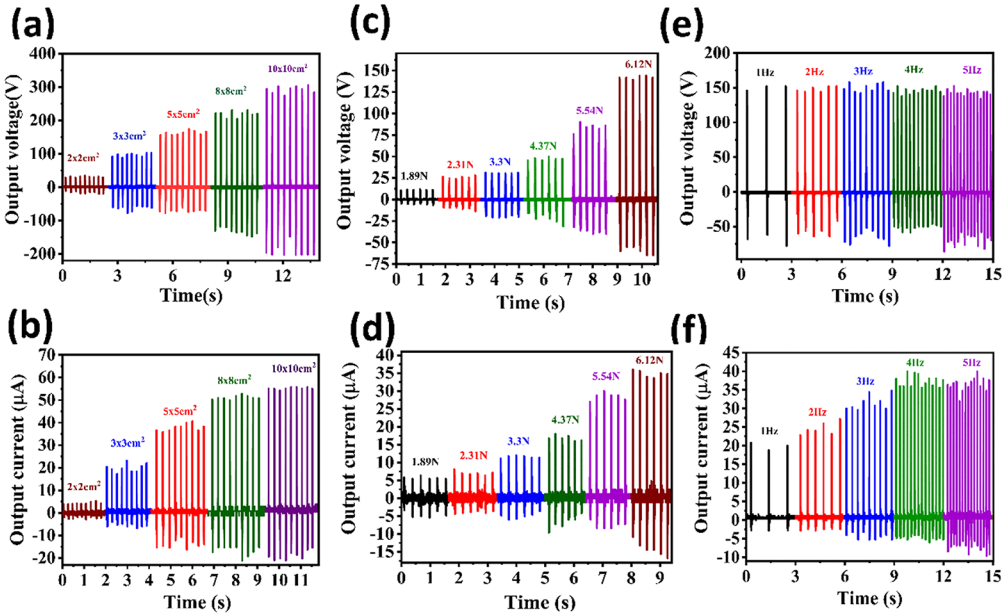

Figure 5. Comparative study of the TENG's open-circuit voltage and short circuit with (a, b) different active areas of the devices, (c, d) different magnitudes of applied forces, and (e, f) different frequencies of the applied force.

load resistance, the average value of V_o increases and I_s decreases, as shown in Figure 3h. From Figure 3h, instantaneous power density was measured using $P = \frac{VI}{A}$ where I and V are the current and voltage at different loads, respectively, and A is the active contact area. The output power density of the TENG is initially increased, reaches the maximum value at optimal load resistance (~4 MΩ), and is decreased for later load resistances, as shown in Figure 3i. The TENG exhibits the highest power density when the external load is equivalent to the device's internal resistance. A maximum power density of 424.8 mW/m^2 is observed at an optimal load resistance of 4 MΩ. The energy conversion efficiency of the TENG was calculated using the calculation procedure reported in the literature.[57−59] The efficiency of the TENG device is defined as the ratio of electrical energy delivered by the TENG to the applied mechanical energy. An energy conversion efficiency of ~6.3% was obtained with the fabricated TENG.

The stability of the fabricated TENG has been tested over a large number of cycles with hand slapping (4300 cycles) and also with the linear motor (>10,000 cycles). The TENG output voltage responses are presented in Figure 4a,b for hand slapping and the linear motor. In the case of hand slapping, sets of ~30−40 cycles of responses were recorded with a gap of a few seconds and all such data sets merged to make 4300 cycles. In the case of the linear motor, the TENG device was continuously tested for 60 min (a frequency of ~3 Hz), and responses were collected at different time intervals such as the 10, 20, 30, 40, 50, and 60th minute (Video S3). The different output voltages in the stability test (Figure 4a,b) are due to the difference in the magnitude of the force applied by the hand slapping and liner motor tapping.

Figure 4c shows the variation of output voltage as a function of the cycle number (every 100th cycle). Furthermore, the TENG's stability was tested over 6 months, as shown in Figure 4d, and was found stable. We have taken SEM images of the ZnO nanosheet film after 10,000 cycle tests to check the stability of the ZnO nanosheets. The SEM images of ZnO nanosheets at different magnifications are shown in Figure S10. The important observations from SEM images are (i) ZnO nanosheets are intact with the substrate, (ii) there were no significant changes in the morphology of ZnO nanosheets, and (iii) at a few places, ZnO nanosheets merged themselves, and this needs a detailed systematic study for better understanding. The stability tests show that the TENG showed a highly stable output over a long period of time.

To know the best performance of the TENG, we have studied the effect of the different active areas of devices, different frequencies of applied forces, and different magnitudes of applied forces. Figure 5 represents a comparative study of the TENG's open-circuit voltage and short-circuit current under the effect of different parameters. Figure 5a,b shows the variation of the TENG output voltage and current with different active areas of 2 × 2, 3 × 3, 5 × 5, 8 × 8, and 10 × 10 cm^2.

It is clear from Figure 5a,b that the TENG output voltage and current are increased with the active area of the devices. As the active area of the device increases, the effective contact electrification also increases proportionally, which results in the increase in voltage and current. The reported literature well supports the observed behavior of the TENG with the area of the devices.[60,61] Further, the effect of applied hand slapping force on the TENG output was studied and is presented in Figure 5c,d. The TENG output voltage and the current are increased gradually with the applied force. This could be due to the increased friction area between the triboelectric layers with applied force, resulting in more charges. A similar dependence of TENG performance with applied force is observed for the other TENGs in the literature.[61,62]Figure 5e,f represents the variation of TENG output voltage and the current with different frequencies of applied force. The output voltage did not change much with frequency, and this may be due to the fact that the open-circuit voltage does not involve any dynamic charge process under open-circuit conditions.[63,64] On the other hand, the current increased with frequency and stabilized after 4 Hz. The output current is increased due to the fast transferring of charges at high frequency of contact and separation.[63]

https://doi.org/10.1021/acsaem.2c02359
ACS Appl. Energy Mater. 2022, 5, 13702−13713

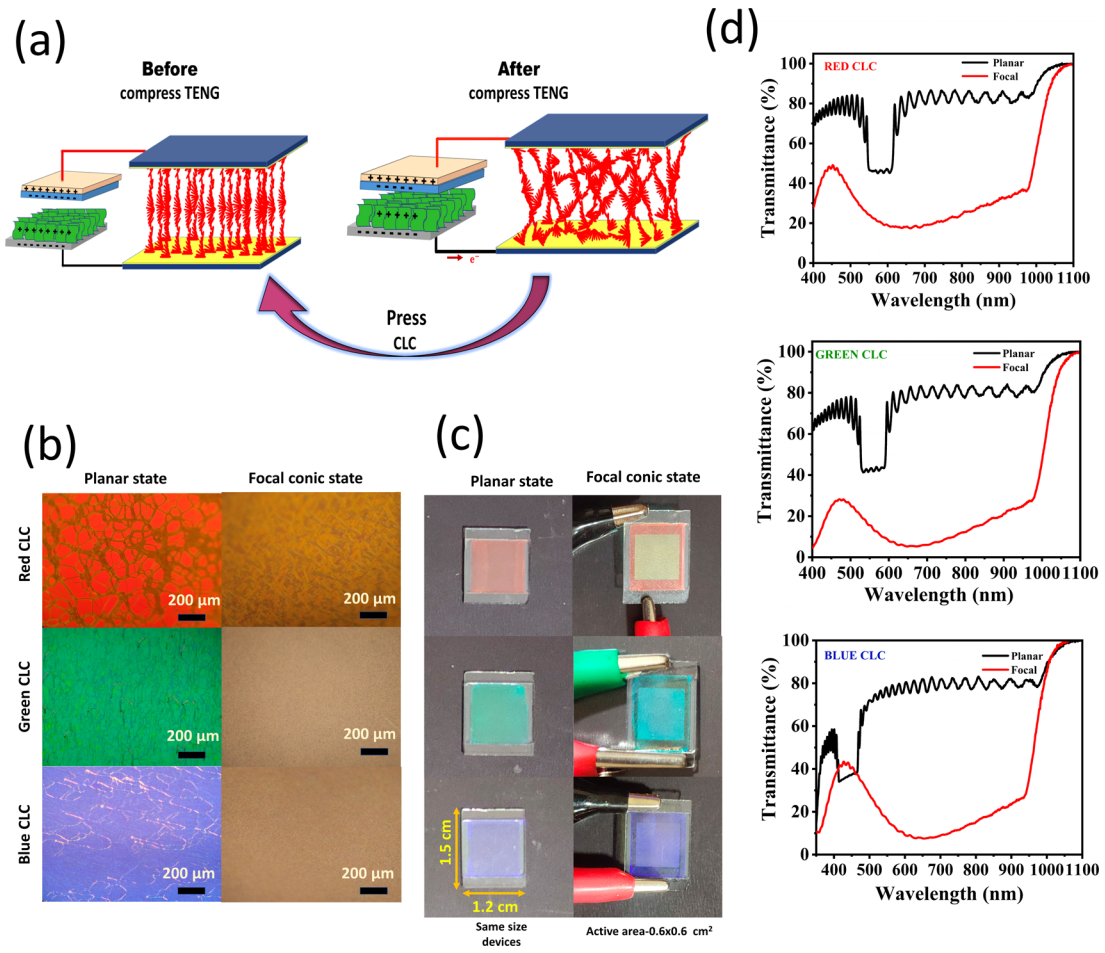

Figure 6. (a) Working principle of the self-powered CLC device driven with the TENG device before and after applying force on the TENG, (b) polarizing optical microscopy images of different CLCs in red, blue, and green cells driven from planar to focal conic by the TENG device, (c) real-time images of different CLCs in red, blue, and green cells driven from planar to focal conic by the TENG device, and (d) transmission spectra of CLC devices in the planar and focal conic state.

4. APPLICATIONS OF TENG

4.1. Self-Powered CLC Device Applications. Figure 6a illustrates the switching mechanism of the CLC device between planar and focal conic textures induced by the AC electrical signal from the TENG. The applied AC signal can change the orientation of the molecules and thus affect their optical properties. In this manuscript, CLC devices are driven directly by the AC output of the TENG, which affects their optical properties. It is essential to have a higher input voltage to switch the CLC device from a planar to a focal conic state. Therefore, a 10 × 10 cm^2 TENG device was used for this application. An open-circuit voltage and short-circuit current of ~292 V and 55 μA, respectively, were observed for the 10 × 10 cm^2 TENG, as shown in Figure S11.

Initially, CLCs are in the planar (P) state, in which they exhibit a partially transparent state. In this state, only a particular wavelength of light in the width of the CLC's photonic bandgap is transmitted, and the rest is reflected. When the TENG's electrical pulse is applied, the CLCs are changed from a planar (P) to a focal conic (FC) state, in which the helicoidal CLC structure is randomly orientated, scattering incident light and causing the display to become opaque (Video S4). The CLC FC state can be changed back to the planar state after the applied force on the TENG device is released. The polarized microscopic images and real-time photographs of the CLC devices are shown in Figure 6b and Figure 6c, respectively, which depicts the transformation of CLC devices from the P to FC when the AC output of the TENG is applied. Figure 6d shows the transmission spectra of the CLC devices in the planar state and focal conic state triggered by the TENG. It is clear that the transmitted light intensity has decreased in the FC state.

The arrangement of the LC molecules inside the cell determines their collective optical properties. For example, when the molecules are arranged in a planar (P) alignment that is parallel to the substrate, the layer reflects light of specific wavelengths depending on the pitch and is transparent for the rest of the wavelengths. Therefore, when no voltage is applied, the planar state is semi-transparent to light. The intermolecular forces are rather weak and can be perturbed by an applied electric field. Because the molecules are polar, they interact with an electric field, which causes them to change their orientation slightly.[65−67] When an electric field was applied to the cholesteric liquid crystal (CLC) cell, the helical pitch and direction of the LC were changed from their initial states because of the compromise between the dielectric and elastic torques. When the planar state is subjected to an AC voltage, it changes to the focal conic state. If the applied voltage is not enough to unwind the helix, then the LC molecules try to align in the direction of the applied electric field. As a result, the helices tilt away from the substrate without unwinding the helix. Since

https://doi.org/10.1021/acsaem.2c02359
ACS Appl. Energy Mater. 2022, 5, 13702−13713

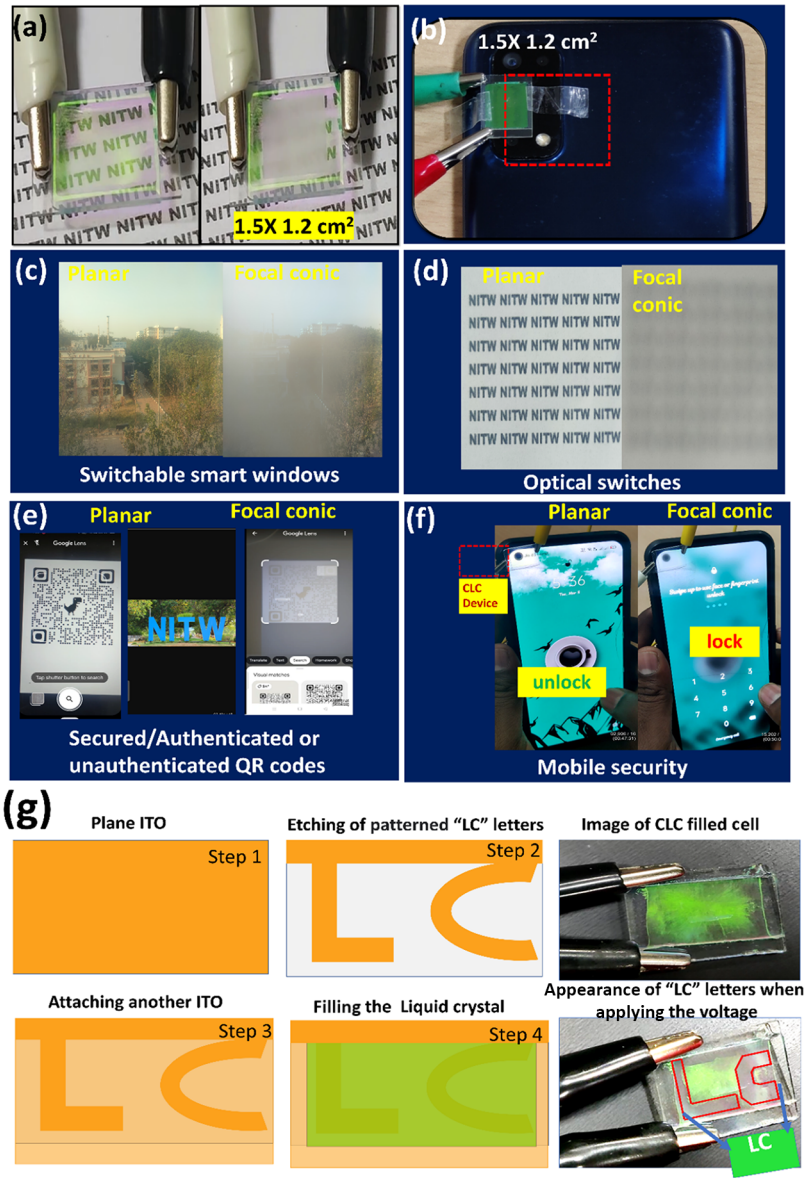

Figure 7. (a) Switching action of the CLC, (b) photograph of the CLC device integrated with a mobile phone camera; practical applications of CLC devices integrated with the TENG are (c) switchable smart windows, (d) optical switches, (e) secured/authenticated or unauthenticated QR codes, (f) mobile phone face lock security, and (g) display of patterned "LC" letters of the CLC connected to the TENG device.

the helix is randomly oriented, it scatters light.[66,67] Therefore, the focal conic state is opaque to light.

We attempted to investigate real-time applications by exploiting the partial transmittance in the P state and opaqueness in the FC state of the CLC device. Secure authentication devices (facial unlocking in mobile phones, QR code scanning, etc.), smart windows, and a CLC display to show letters are all real-time applications (optical switch) (Videos S5–S8).

The primary switching action of a self-powered CLC device is shown in Figure 7a. The CLC device was placed over a text printed paper, and the visibility of the text through the CLC device in the P and FC state clearly demonstrates the switching action (Video S5). To exemplify the potential of CLC devices for smart window applications, we have installed the CLC device on top of the smartphone camera, as shown in Figure 7b and captured images. We used the smartphone camera to photograph the landscape of a building before and after applying the TENG pulse to it using a CLC device, as shown in Figure 7c (Video S6). When the CLC device is in the P state, the scenery of the building is clear; nevertheless, when the CLC device is converted to the FC state by the TENG electrical pulse, the scenery of the building is not apparent. To demonstrate the CLC device as an optical switch, we have captured the text (NITW) printed on a paper through the CLC device via the smartphone camera before and after applying the TENG pulse, as shown in Figure 7d. We also have tried to scan the QR code before applying the TENG pulse to the CLC device, and the QR code has been scanned successfully and shows the encoded picture with "NITW" letters, as shown in Figure 7e. When the TENG output was applied to the CLC device, the QR code could not be scanned due to the CLC device's transition to the FC state. This results in other misleading results on the Google lens (mobile) app, as shown in Figure 7e (Video S7). In a similar way, we have tried to unlock a smartphone using the face recognition unlock method. When the TENG device was pressed, the smartphone

https://doi.org/10.1021/acsaem.2c02359
ACS Appl. Energy Mater. 2022, 5, 13702−13713

was locked, but before applying the TENG, the smartphone was unlocked successfully, as shown in Figure 7f (Video S8). In this way, this self-powered CLC-TENG is helpful as a security device.

We also have demonstrated a self-powered CLC for text display applications. We have patterned "LC" letters on the ITO plate by using a simple etching procedure, as shown in Figure 7g. Initially, the pattern "LC" was masked using a Kapton tape, and the unpatterned area can be etched out using a concentrated solution of HCl and Zinc dust. Later, the ITO plates were washed thoroughly, spin-coated with PVA solution, and baked at 200 °C for 2 h. The cell was made by maintaining a gap of 5 μm using PET films, and the CLC was filled through capillary action. The CLC cell exhibited a green reflection shown in Figure 7g; however, when the TENG pulse was applied, the display showed "LC" letters in the transparent state (whitish color) owing to the change of the CLC to the FC state, but the etched region still showed a green reflection (Video S9).

4.2. Self-Powered Electroluminescence and Portable Electronic Device Application. Furthermore, the TENG AC output has been used for powering electroluminescence (EL) devices. Figure 8a shows the schematic structure of the

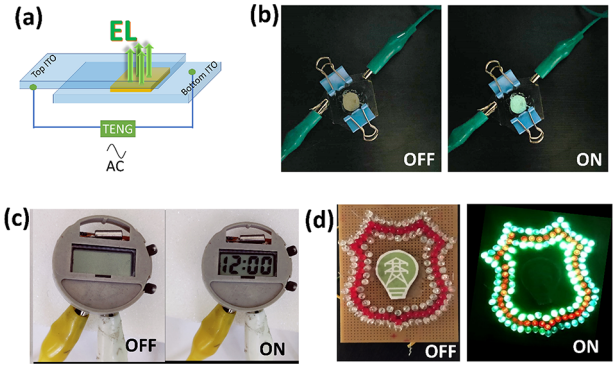

Figure 8. (a) Schematic of the electroluminescence device and its components; on and off state photographs of (b) electroluminescence, (c) digital watch, and (d) LEDs.

electroluminescence device in which luminescent powder (ZnS-Cu, Al) is sandwiched between two ITO electrodes without any short circuit. The output of the TENG device was given directly to the EL device's top and bottom ITO electrodes. Figure 8b shows the photographs of the electroluminescence device before and after applying a TENG output (Video S10). A very high electric field (10^6 to 10^7 V/m) is required to obtain AC-EL emission from the ZnS:Cu, Al phosphor material. The phosphor with a particle size of less than 20 μm can induce such a local field when a potential difference of more than 100 V_{PP} (peak to peak) is applied across the EL device. In practical phosphors, the radiative emission is not caused by direct recombination but by transitions taking place via energy levels of activators introduced as impurities. In ZnS:Cu, Al phosphor, the excess doping of copper (~1000−1500 ppm) is a prerequisite for the phosphor to exhibit EL. This has the dual functionality of primarily forming electrically conducting Cu_xS needles inside the ZnS grain and, second, creating the luminescence centers required in the ZnS host lattice.[68,69] When a high voltage is applied, the Cu_xS needles provide an enhanced local electric field in the ZnS grains, thus producing EL. The field emission of electrons from the sharp ends of Cu-rich conducting Cu_xS needles occurs at alternate ends as the field reverses. These electrons are trapped at some short distance from the inclusion. They are then released from the traps when the field is sufficiently high and accelerated toward the inclusion where the field enhancement causes impact ionization, leaving behind a hole. These electrons can drift through the bulk and subsequently recombine radiatively within the trapped holes. Finally, radiative relaxation results in AC-EL. The fabricated TENG is capable of producing visible electroluminescence from the EL device. In addition, we can design self-powered electroluminescence signboards/ text displays using large-area TENG devices.

We have tested the fabricated TENG further to directly power the digital watch and 135 series-connected LEDs (Videos S11 and S12, respectively). Figure 8c and Figure 8d show the photographs of the digital watch and LEDs before and after applying the TENG output to them, respectively.

Figure 9a shows the charging curves of different load capacitors (1−440 μF) by continuous operation of the TENG for ~380 s. The TENG output was rectified using a full wave rectifier (DB107), and the rectified output is shown in Figure S12. The rectified TENG output was used for charging the capacitors. From the charging curves, it is concluded that the capacitors are charged in the range of 0.2−9 V in 280 s. The charging speed is higher for a smaller load capacitor and quickly reaches the saturation voltage (V). On the other hand, the charging speed is slow for a higher load capacitor, and it may reach saturation voltage at a longer time duration. From the charge and potential difference relationship equation $Q = C_L V$, the stored charge was calculated and is presented in Figure 9b. As expected, the stored charge in the capacitor increased with the load capacitor values. The 440 μF load capacitor held the maximum charges of ~150 μc in 300 s. The output voltage and stored charge were plotted as a function of the load capacitance, which is shown in Figure 9c. It indicates an inverse relationship between the output voltage and the stored charge with respect to the load capacitance.

In addition, the stored energy was calculated from $E = \frac{1}{2}CV^2$ and is shown in Figure 9d. The maximum stored energy is observed at an optimal load capacitance value of 47 μF, where the impedance between the TENG and the capacitive load matches. The load capacitance behavior of the TENG is similar to the existing literature. We have further powered the electronic calculator and digital thermometer by utilizing the charged voltage of the 4.7 μF capacitor in less than 30 s (Videos S13 and S14, respectively). The charging and discharging of the capacitor before and after the load is connected are shown in Figure 9e,f.

5. CONCLUSIONS

In conclusion, a novel and high-performance TENG has been utilized for self-powered cholesteric liquid crystal, electroluminescence, and portable electronic devices. The cost-effective TENG was fabricated using ZnO nanosheet films and OHP sheets. The fabricated TENG produced a high output voltage, current, and power density of ~292 V, ~55 μA, and ~424.8 mW/m^2, respectively. The self-powered CLC is used for security, display, and smart window applications. The self-powered electroluminescence devices and LEDs can be used for e-paper/digital billboard applications. This real-time proof-of-concept study showed the combination of the TENG with the CLC and EL for intelligent mechanical responsive devices, and this area offers a lot of room for growth.

https://doi.org/10.1021/acsaem.2c02359
ACS Appl. Energy Mater. 2022, 5, 13702−13713

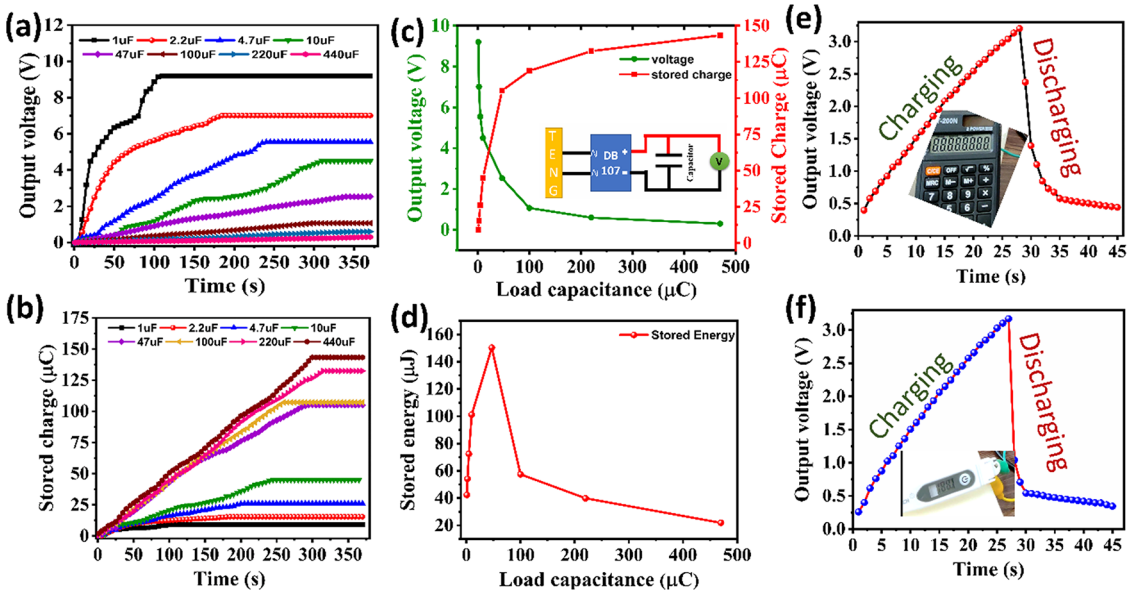

Figure 9. (a) Charging curves of different load capacitors, (b) stored charge at different load capacitances, (c) output voltage and stored charge behavior as a function of the load capacitance, (d) maximum stored energy as a function of the load capacitance; charging and discharging curves of the 4.7 μF capacitor before and after connecting the (e) calculator and (f) digital thermometer.

■ ASSOCIATED CONTENT

Supporting Information

The Supporting Information is available free of charge at https://pubs.acs.org/doi/10.1021/acsaem.2c02359.

Confirmation of the charged state of the OHP sheet surface; TENG cost and OHP sheet details; experimental details; TENG fabrication and mechanism; other characterization details; TENG device with the OHP sheet of different manufacturers; SEM images of ZnO nanosheets after the stability test; response of the 10 × 10 cm^2 device, and rectified voltage of the TENG (PDF)

Video S1: Charge nature of the pre-charged (OHP) PET and normal PET (MP4)

Video S2: Charge confirmation of the OHP sheet on both sides (MP4)

Video S3: A stability test with a linear motor at different points in time (MP4)

Video S4: Switching of the CLC device planar to the focal conic state (MP4)

Video S5: Optical switching of NITW letters by using the TENG (MP4)

Video S6: A switchable smart window by using the TENG (MP4)

Video S7: QR code scanning by the TENG in planar and focal states (MP4)

Video S8: Mobile phone face lock security (MP4)

Video S9: Switching of the "LC" letter pattern using the TENG (MP4)

Video S10: Demonstration of EL device lighting (MP4)

Video S11: Demonstration of the digital watch display (MP4)

Video S12: LEDs lighting up by the TENG (MP4)

Video S13: Powering of the calculator (MP4)

Video S14: Powering of the thermometer (MP4)

■ AUTHOR INFORMATION

Corresponding Author

Rakesh Kumar Rajaboina − *Department of Physics, Energy Materials and Devices Lab, National Institute of Technology, Warangal 506004, India;* orcid.org/0000-0003-4023-9051; Email: rakeshr@nitw.ac.in

Authors

Supraja Potu − *Department of Physics, Energy Materials and Devices Lab, National Institute of Technology, Warangal 506004, India;* orcid.org/0000-0001-5612-4035

Navaneeth M − *Department of Physics, Energy Materials and Devices Lab, National Institute of Technology, Warangal 506004, India;* orcid.org/0000-0002-2001-9038

Buchaiah Gollapelli − *Department of Physics, Liquid Crystals Research Lab, National Institute of Technology, Warangal 506004, India;* orcid.org/0000-0001-6987-9429

Jayalakshmi Vallamkondu − *Department of Physics, Liquid Crystals Research Lab, National Institute of Technology, Warangal 506004, India;* orcid.org/0000-0002-5259-6286

Siju Mishra − *Department of Physics, Energy Materials and Devices Lab, National Institute of Technology, Warangal 506004, India;* orcid.org/0000-0003-3774-4196

Haranath Divi − *Department of Physics, Energy Materials and Devices Lab, National Institute of Technology, Warangal 506004, India;* orcid.org/0000-0002-7936-6165

Anjaly Babu − *Department of Physics, Energy Materials and Devices Lab, National Institute of Technology, Warangal 506004, India;* orcid.org/0000-0001-9569-7442

Uday Kumar K − *Department of Physics, Energy Materials and Devices Lab, National Institute of Technology, Warangal 506004, India;* orcid.org/0000-0003-1297-4104

Prakash Kodali − *Department of Electronics and Communication Engineering, Flexible Electronics Lab, National Institute of Technology, Warangal 506004, India;* orcid.org/0000-0001-9009-7325

Complete contact information is available at:

https://doi.org/10.1021/acsaem.2c02359
ACS Appl. Energy Mater. 2022, 5, 13702−13713

https://pubs.acs.org/10.1021/acsaem.2c02359

Notes

The authors declare no competing financial interest.

■ ACKNOWLEDGMENTS

The authors would like to thank the Department of Physics and Centre for Research and Instrument facility (CRIF), NIT-Warangal, for providing their research facilities. The authors would like to thank Dr. Syam Prasad and Dr. Paul Joseph for extending their lab facilities for UV−vis measurements.

■ REFERENCES

(1) Wu, C.; Wang, A. C.; Ding, W.; Guo, H.; Wang, Z. L. Triboelectric Nanogenerator: A Foundation of the Energy for the New Era. *Adv. Energy Mater.* **2019**, *9*, 1−25.
(2) Yu, A.; Jiang, P.; Lin Wang, Z. Nanogenerator as Self-Powered Vibration Sensor. *Nano Energy* **2012**, *1*, 418−423.
(3) Wang, H.; Cheng, J.; Wang, Z.; Ji, L.; Wang, Z. L. Triboelectric Nanogenerators for Human-Health Care. *Sci. Bull.* **2021**, *66*, 490−511.
(4) Yeh, M. H.; Lin, L.; Yang, P. K.; Wang, Z. L. Motion-Driven Electrochromic Reactions for Self-Powered Smart Window System. *ACS Nano* **2015**, *9*, 4757−4765.
(5) Park, H. J.; Kim, S.; Lee, J. H.; Kim, H. T.; Seung, W.; Son, Y.; Kim, T. Y.; Khan, U.; Park, N. M.; Kim, S. W. Self-Powered Motion-Driven Triboelectric Electroluminescence Textile System. *ACS Appl. Mater. Interfaces* **2019**, *11*, 5200−5207.
(6) Chen, X.; Wu, Y.; Yu, A.; Xu, L.; Zheng, L.; Liu, Y.; Li, H.; Lin Wang, Z. Self-Powered Modulation of Elastomeric Optical Grating by Using Triboelectric Nanogenerator. *Nano Energy* **2017**, *38*, 91−100.
(7) Jiang, D.; Fan, Z.; Wang, H.; Xu, M.; Chen, G.; Song, Y.; Wang, Z. L. Triboelectric Nanogenerator Powered Electrowetting-on-Dielectric Actuator for Concealed Aquatic Microbots. *ACS Nano* **2020**, *14*, 15394−15402.
(8) Gu, Y.; Hou, T.; Chen, P.; Cao, J.; Pan, C.; Hu, W.; Yang, B.-R.; Pu, X.; Wang, Z. L. Self-Powered Electronic Paper with Energy Supplies and Information Inputs Solely from Mechanical Motions. *Photonics Res.* **2020**, *8*, 1496.
(9) Fan, F. R.; Tian, Z. Q.; Lin Wang, Z. Flexible Triboelectric Generator. *Nano Energy* **2012**, *1*, 328−334.
(10) Saravanakumar, B.; Thiyagarajan, K.; Alluri, N. R.; SoYoon, S.; Taehyun, K.; Lin, Z. H.; Kim, S. J. Fabrication of an Eco-Friendly Composite Nanogenerator for Self-Powered Photosensor Applications. *Carbon* **2015**, *84*, 56−65.
(11) Shao, J. J.; Jiang, T.; Wang, Z. L. Theoretical Foundations of Triboelectric Nanogenerators (TENGs). *Sci. China Technol. Sci.* **2020**, *63*, 1087−1109.
(12) Pan, S.; Zhang, Z. Fundamental Theories and Basic Principles of Triboelectric Effect: A Review. *Friction* **2019**, *7*, 2−17.
(13) Niu, S.; Wang, S.; Lin, L.; Liu, Y.; Zhou, Y. S.; Hu, Y.; Wang, Z. L. Theoretical Study of Contact-Mode Triboelectric Nanogenerators as an Effective Power Source. *Energy Environ. Sci.* **2013**, *6*, 3576−3583.
(14) Zou, H.; Guo, L.; Xue, H.; Zhang, Y.; Shen, X.; Liu, X.; Wang, P.; He, X.; Dai, G.; Jiang, P.; Zheng, H. Quantifying and understanding the triboelectric series of inorganic non-metallic materials. *Nat. Commun.* **2020**, *11*, No. 2093.
(15) Zhao, Z.; Zhou, L.; Li, S.; Liu, D.; Li, Y.; Gao, Y.; Liu, Y.; Dai, Y.; Wang, J.; Wang, Z. L. Selection Rules of Triboelectric Materials for Direct-Current Triboelectric Nanogenerator. *Nat. Commun.* **2021**, *12*, 1−8.
(16) Kaur, J.; Singh, H. Fabrication of Composite Material Based Nanogenerator for Electricity Generation Enhancement of Food Waste By-Product. *Mater. Chem. Phys.* **2020**, *256*, No. 123331.
(17) Zhang, R.; Olin, H. Material Choices for Triboelectric Nanogenerators: A Critical Review. *EcoMat* **2020**, *2*, 1−13.
(18) Zhao, L.; Zheng, Q.; Ouyang, H.; Li, H.; Yan, L.; Shi, B.; Li, Z. A Size-Unlimited Surface Microstructure Modification Method for Achieving High Performance Triboelectric Nanogenerator. *Nano Energy* **2016**, *28*, 172−178.
(19) Fan, F. R.; Lin, L.; Zhu, G.; Wu, W.; Zhang, R.; Wang, Z. L. Transparent Triboelectric Nanogenerators and Self-Powered Pressure Sensors Based on Micropatterned Plastic Films. *Nano Lett.* **2012**, *12*, 3109−3114.
(20) Lin, Z. H.; Xie, Y.; Yang, Y.; Wang, S.; Zhu, G.; Wang, Z. L. Enhanced Triboelectric Nanogenerators and Triboelectric Nanosensor Using Chemically Modified TiO2 Nanomaterials. *ACS Nano* **2013**, *7*, 4554−4560.
(21) Song, G.; Kim, Y.; Yu, S.; Kim, M. O.; Park, S. H.; Cho, S. M.; Velusamy, D. B.; Cho, S. H.; Kim, K. L.; Kim, J.; Kim, E.; Park, C. Molecularly Engineered Surface Triboelectric Nanogenerator by Self-Assembled Monolayers (METS). *Chem. Mater.* **2015**, *27*, 4749−4755.
(22) Shin, S. H.; Kwon, Y. H.; Kim, Y. H.; Jung, J. Y.; Lee, M. H.; Nah, J. Triboelectric Charging Sequence Induced by Surface Functionalization as a Method to Fabricate High Performance Triboelectric Generators. *ACS Nano* **2015**, *9*, 4621−4627.
(23) Ravichandran, A. N.; Ramuz, M.; Blayac, S. Increasing Surface Charge Density by Effective Charge Accumulation Layer Inclusion for High-Performance Triboelectric Nanogenerators. *MRS Commun.* **2019**, *9*, 682−689.
(24) Wang, S.; Xie, Y.; Niu, S.; Lin, L.; Liu, C.; Zhou, Y. S.; Wang, Z. L. Maximum Surface Charge Density for Triboelectric Nanogenerators Achieved by Ionized-Air Injection: Methodology and Theoretical Understanding. *Adv. Mater.* **2014**, *26*, 6720−6728.
(25) Kim, W.; Okada, T.; Park, H. W.; Kim, J.; Kim, S.; Kim, S. W.; Samukawa, S.; Choi, D. Surface Modification of Triboelectric Materials by Neutral Beams. *J. Mater. Chem. A* **2019**, *7*, 25066−25077.
(26) Li, H. Y.; Su, L.; Kuang, S. Y.; Pan, C. F.; Zhu, G.; Wang, Z. L. Significant Enhancement of Triboelectric Charge Density by Fluorinated Surface Modification in Nanoscale for Converting Mechanical Energy. *Adv. Funct. Mater.* **2015**, *25*, 5691−5697.
(27) Chen, J.; Guo, H.; He, X.; Liu, G.; Xi, Y.; Shi, H.; Hu, C. Enhancing Performance of Triboelectric Nanogenerator by Filling High Dielectric Nanoparticles into Sponge PDMS Film. *ACS Appl. Mater. Interfaces* **2016**, *8*, 736−744.
(28) Ali, D.; Yu, B.; Duan, X.; Yu, H.; Zhu, M.Enhancement of Output Performance through Post-Poling Technique on BaTiO3/PDMS-Based Triboelectric Nanogenerator. *Nanotechnology***2017**, *28*. 075203
(29) He, X.; Guo, H.; Yue, X.; Gao, J.; Xi, Y.; Hu, C. Improving Energy Conversion Efficiency for Triboelectric Nanogenerator with Capacitor Structure by Maximizing Surface Charge Density. *Nanoscale* **2015**, *7*, 1896−1903.
(30) Tang, W.; Jiang, T.; Fan, F. R.; Yu, A. F.; Zhang, C.; Cao, X.; Wang, Z. L. Liquid-Metal Electrode for High-Performance Triboelectric Nanogenerator at an Instantaneous Energy Conversion Efficiency of 70.6%. *Adv. Funct. Mater.* **2015**, *25*, 3718−3725.
(31) Cheng, P.; Guo, H.; Wen, Z.; Zhang, C.; Yin, X.; Li, X.; Liu, D.; Song, W.; Sun, X.; Wang, J.; Wang, Z. L. Largely Enhanced Triboelectric Nanogenerator for Efficient Harvesting of Water Wave Energy by Soft Contacted Structure. *Nano Energy* **2018**, *2019*, 432−439.
(32) Wang, J.; Meng, C.; Wang, C. T.; Liu, C. H.; Chang, Y. H.; Li, C. C.; Tseng, H. Y.; Kwok, H. S.; Zi, Y. A Fully Self-Powered, Ultra-Stable Cholesteric Smart Window Triggered by Instantaneous Mechanical Stimuli. *Nano Energy* **2021**, *85*, No. 105976.
(33) Chen, Y. H.; Lin, P. Y.; Wang, T. W.; Tiwari, N.; Lin, S. C.; Wu, H. S.; Choi, D.; Wu, W.; Choi, D.; Hsiao, Y. C.; Lin, Z. H. Dynamics of Electrically Driven Cholesteric Liquid Crystals by Triboelectrification and Their Application in Self-Powered Information Securing and Vision Correcting. *ACS Energy Lett.* **2021**, *6*, 3185−3194.
(34) Wang, J.; Meng, C.; Gu, Q.; Tseng, M. C.; Tang, S. T.; Kwok, H. S.; Cheng, J.; Zi, Y. Normally Transparent Tribo-Induced Smart Window. *ACS Nano* **2020**, *14*, 3630−3639.
(35) Liu, H.; Guo, Z. H.; Xu, F.; Jia, L.; Pan, C.; Wang, Z. L.; Pu, X. Triboelectric-Optical Responsive Cholesteric Liquid Crystals for Self-Powered Smart Window, E-Paper Display and Optical Switch. *Sci. Bull.* **2021**, *66*, 1986−1993.

(36) Pu, X.; Zha, J. W.; Zhao, C. L.; Gong, S. B.; Gao, J. F.; Li, R. K. Y. Flexible PVDF/Nylon-11 Electrospun Fibrous Membranes with Aligned ZnO Nanowires as Potential Triboelectric Nanogenerators. *Chem. Eng. J.* **2020**, *398*, No. 125526.
(37) Yue, X.; Xi, Y.; Hu, C.; He, X.; Dai, S.; Cheng, L.; Wang, G. Enhanced Output-Power of Nanogenerator by Modifying PDMS Film with Lateral ZnO Nanotubes and Ag Nanowires. *RSC Adv.* **2015**, *5*, 32566−32571.
(38) Li, D.; Wu, C.; Ruan, L.; Wang, J.; Qiu, Z.; Wang, K.; Liu, Y.; Zhang, Y.; Guo, T.; Lin, J.; Kim, T. W. Electron-Transfer Mechanisms for Confirmation of Contact-Electrification in ZnO/Polyimide-Based Triboelectric Nanogenerators. *Nano Energy* **2020**, *75*, No. 104818.
(39) Ko, Y. H.; Nagaraju, G.; Lee, S. H.; Yu, J. S. PDMS-Based Triboelectric and Transparent Nanogenerators with ZnO Nanorod Arrays. *ACS Appl. Mater. Interfaces* **2014**, *6*, 6631−6637.
(40) Liu, B.; Wang, S.; Yuan, Z.; Duan, Z.; Zhao, Q.; Zhang, Y.; Su, Y.; Jiang, Y.; Xie, G.; Tai, H. Novel Chitosan/ZnO Bilayer Film with Enhanced Humidity-Tolerant Property: Endowing Triboelectric Nanogenerator with Acetone Analysis Capability. *Nano Energy* **2020**, *78*, No. 105256.
(41) Gupta, A. K.; Hsu, C.-H.; Lai, S.-N.; Lai, C.-S. ZnO-Polystyrene Composite as Efficient Energy Harvest for Self-Powered Triboelectric Nanogenerator. *ECS J. Solid State Sci. Technol.* **2020**, *9*, 115019.
(42) Supraja, P.; Kumar, R. R.; Mishra, S.; Haranath, D.; Sankar, P. R.; Prakash, K.; Jayarambabu, N.; Rao, T. V.; Kumar, K. U. A Simple and Low-Cost Triboelectric Nanogenerator Based on Two Dimensional ZnO Nanosheets and Its Application in Portable Electronics. *Sensors Actuators A Phys.* **2022**, *335*, No. 113368.
(43) Jakmuangpak, S.; Prada, T.; Mongkolthanaruk, W.; Harnchana, V.; Pinitsoontorn, S. Engineering Bacterial Cellulose Films by Nanocomposite Approach and Surface Modification for Biocompatible Triboelectric Nanogenerator. *ACS Appl. Electron. Mater.* **2020**, *2*, 2498−2506.
(44) Sahu, M.; Šafranko, S.; Hajra, S.; Padhan, A. M.; Živković, P.; Jokić, S.; Kim, H. J. Development of Triboelectric Nanogenerator and Mechanical Energy Harvesting Using Argon Ion-Implanted Kapton, Zinc Oxide and Kapton. *Mater. Lett.* **2021**, *301*, 1−5.
(45) Supraja, P.; Rakesh Kumar, R.; Mishra, S.; Haranath, D.Triboelectric Nanogenerator Based on ZnO Nanosheet Networks for Mechanical Energy Harvesting. *2022 2nd Int. Conf. Power Electron. IoT Appl. Renew. Energy its Control*; PARC2022,*2022*, 1−4. DOI: 10.1109/PARC52418.2022.9726684.
(46) Singh, H. H.; Khare, N. Flexible ZnO-PVDF/PTFE Based Piezo-Tribo Hybrid Nanogenerator. *Nano Energy* **2018**, *51*, 216−222.
(47) Jeon, Y. P.; Park, J. H.; Kim, T. W. Highly Flexible Triboelectric Nanogenerators Fabricated Utilizing Active Layers with a ZnO Nanostructure on Polyethylene Naphthalate Substrates. *Appl. Surf. Sci.* **2018**, *2019*, 210−214.
(48) Jeon, Y. P.; Park, J. H.; Kim, T. W. Highly-Enhanced Triboelectric Nanogenerators Based on Zinc-Oxide Nanoripples Acting as a Triboelectric Layer. *Appl. Surf. Sci.* **2018**, *445*, 50−55.
(49) Chen, S. N.; Chen, C. H.; Lin, Z. H.; Tsao, Y. H.; Liu, C. P. On Enhancing Capability of Tribocharge Transfer of ZnO Nanorod Arrays by Sb Doping for Anomalous Output Performance Improvement of Triboelectric Nanogenerators. *Nano Energy* **2018**, *45*, 311−318.
(50) Deng, W.; Zhang, B.; Jin, L.; Chen, Y.; Chu, W.; Zhang, H.; Zhu, M.; Yang, W. Enhanced Performance of ZnO Microballoon Arrays for a Triboelectric Nanogenerator. *Nanotechnology* **2017**, *28*, 135401.
(51) Dos Santos, A.; Sabino, F.; Rovisco, A.; Barquinha, P.; Águas, H.; Fortunato, E.; Martins, R.; Igreja, R. Optimization of Zno Nanorods Concentration in a Micro-Structured Polymeric Composite for Nanogenerators. *Chemosensors* **2021**, *9*, 1−13.
(52) Supraja, P.; Rakesh Kumar, R.; Mishra, S.; Haranath, D.; Sankar, P. R.; Prakash, K. A Simple and Low-Cost Approach for the Synthesis and Fabrication of ZnO Nanosheet-Based Nanogenerator for Energy Harvesting and Sensing. *Eng. Res. Express* **2021**, *3*, No. 035022.
(53) Sultana, A.; Alam, M. M.; Garain, S.; Sinha, T. K.; Middya, T. R.; Mandal, D. An Effective Electrical Throughput from PANI Supplement ZnS Nanorods and PDMS-Based Flexible Piezoelectric Nanogenerator for Power up Portable Electronic Devices: An Alternative of MWCNT Filler. *ACS Appl. Mater. Interfaces* **2015**, *7*, 19091−19097.
(54) Yang, B.; Zeng, W.; Peng, Z. H.; Liu, S. R.; Chen, K.; Tao, X. M. A Fully Verified Theoretical Analysis of Contact-Mode Triboelectric Nanogenerators as a Wearable Power Source. *Adv. Energy Mater.* **2016**, *6*, 1−8.
(55) Zhang, H.; Quan, L.; Chen, J.; Xu, C.; Zhang, C.; Dong, S.; Lü, C.; Luo, J. A General Optimization Approach for Contact-Separation Triboelectric Nanogenerator. *Nano Energy* **2019**, *56*, 700−707.
(56) Yang, R.; Qin, Y.; Li, C.; Dai, L.; Wang, Z. L. Characteristics of Output Voltage and Current of Integrated Nanogenerators. *Appl. Phys. Lett.* **2009**, *94*, 92−95.
(57) Zhu, G.; Lin, Z. H.; Jing, Q.; Bai, P.; Pan, C.; Yang, Y.; Zhou, Y.; Wang, Z. L. Toward Large-Scale Energy Harvesting by a Nanoparticle-Enhanced Triboelectric Nanogenerator. *Nano Lett.* **2013**, *13*, 847−853.
(58) Jeong, C. K.; Baek, K. M.; Niu, S.; Nam, T. W.; Hur, Y. H.; Park, D. Y.; Hwang, G. T.; Byun, M.; Wang, Z. L.; Jung, Y. S.; Lee, K. J. Topographically-Designed Triboelectric Nanogenerator via Block Copolymer Self-Assembly. *Nano Lett.* **2014**, *14*, 7031−7038.
(59) You, A.; Zhang, X.; Peng, X.; Dong, K.; Lu, Y.; Zhang, Q. A Skin-Inspired Triboelectric Nanogenerator with an Interpenetrating Structure for Motion Sensing and Energy Harvesting. *Macromol. Mater. Eng.* **2021**, *306*, 2170028.
(60) Kamilya, T.; Sarkar, P. K.; Acharya, S. Unveiling Peritoneum Membrane for a Robust Triboelectric Nanogenerator. *ACS Omega* **2019**, *4*, 17684−17690.
(61) Lu, Y.; Tian, H.; Cheng, J.; Zhu, F.; Liu, B.; Wei, S.; Ji, L.; Wang, Z. L. Decoding Lip Language Using Triboelectric Sensors with Deep Learning. *Nat. Commun.* **2022**, *13*, 1−12.
(62) Rana, S. M. S.; Rahman, M. T.; Salauddin, M.; Sharma, S.; Maharjan, P.; Bhatta, T.; Cho, H.; Park, C.; Park, J. Y. Electrospun PVDF-TrFE/MXene Nanofiber Mat-Based Triboelectric Nanogenerator for Smart Home Appliances. *ACS Appl. Mater. Interfaces* **2021**, *13*, 4955−4967.
(63) Pan, R.; Xuan, W.; Chen, J.; Dong, S.; Jin, H.; Wang, X.; Li, H.; Luo, J. Fully Biodegradable Triboelectric Nanogenerators Based on Electrospun Polylactic Acid and Nanostructured Gelatin Films. *Nano Energy* **2018**, *45*, 193−202.
(64) Wang, S.; Lin, L.; Wang, Z. L. Nanoscale Triboelectric-Effect-Enabled Energy Conversion for Sustainably Powering Portable Electronics. *Nano Lett.* **2012**, *12*, 6339−6346.
(65) Ryabchun, A.; Bobrovsky, A. Cholesteric Liquid Crystal Materials for Tunable Diffractive Optics. *Adv. Opt. Mater.* **2018**, *6*, 1800335.
(66) Bisoyi, H. K.; Li, Q. Liquid Crystals: Versatile Self-Organized Smart Soft Materials. *Chem. Rev.* **2022**, *122*, 4887−4926.
(67) Oh, S. W.; Baek, J. M.; Kim, S. H.; Yoon, T. H. Optical and Electrical Switching of Cholesteric Liquid Crystals Containing Azo Dye. *RSC Adv.* **2017**, *7*, 19497−19501.
(68) Chander, H.; Shanker, V.; Haranath, D.; Dudeja, S.; Sharma, P. Characterization of ZnS:Cu, Br Electroluminescent Phosphor Prepared by New Route. *Mater. Res. Bull.* **2003**, *38*, 279−288.
(69) Haranath, D.; Sahai, S.; Mishra, S.; Husain, M.; Shanker, V.Fabrication and Electro-Optic Properties of a MWCNT Driven Novel Electroluminescent Lamp. *Nanotechnology***2012**, *23*, 435704.